Simulation Report
of the ENA Instrument

Yoichi Kazama

INSTITUTET FÖR RYMDFYSIK
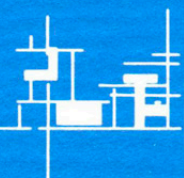### Swedish Institute of Space Physics

Kiruna, Sweden

Simulation Report of the ENA Instrument

Yoichi Kazama

Simulation Report of the ENA Instrument

Yoichi Kazama (yoichi@irf.se)

June 5, 2006

1 Purpose of the Report

The purpose of this document is to describe performances of an energetic neutral atom (ENA) instrument derived from numerical simulations. The instrument is being developed at Institute of Space Physics (Institutet för rymdfysik; IRF) in cooperation with Institute of Space and Astronautical Science (ISAS) in Japan, and University of Bern (UBe) in Switzerland. This instrument has been selected for the Indian Moon exploration mission Chandrayaan-1, and the European-Japanese Mercury exploration mission BepiColombo.

2 Design Driver

Design drivers on developing an ENA instrument are:

- **Light Weight** In planetary exploration, instruments are requested to be light weight. In the case of this ENA instrument, 2 kilograms of weight is a goal.

- **Mass Analysis** Because ENAs around a planet reflect their source information, mass analysis is essential for scientific objectives such as global mapping of surface elements on planets.

- **Noise Reduction** Noise must be suppressed since ENAs are expected to be tenuous. Ambient ions must be swept out before ionization of ENAs not to confuse. To block a large amount of photons is also a key on designing an instrument.

- **Low-Energy ENA Detection** Specially-developed surfaces dedicated to ionizing low-energy ENAs are employed. Non-conductive parts near particle paths are hidden to avoid electric charge-up.

Since we have a strict limitation of the instrument weight, it is obvious that not all performances can be maximized simultaneously. In designing the instrument, we searched an optimum design which satisfies requirements: (1) instrument weight, (2) high sensitivity,

(3) high signal-to-noise ratio, (4) mass discrimination and (5) angular coverage/resolution (in order of priority).

3   Detection Method

To meet the requirements shown above, we carefully designed an ENA instrument. Figure 1 displays a cut-off view of the sensor part of the instrument. The instrument consists of four parts, that is:

- **Charged-Particle Rejector** to sweep out ambient charged particles by applying an electric field, and to define the field of view in elevation.

- **Ionization Surface** to ionize ENAs positively with a certain probability for following electrostatic energy analysis.

- **Wave Structure** to block photons and to make coarse energy analysis.

- **Time-Of-Flight Section** to measure time of flight (TOF) of a particle for velocity analysis, and to suppress noise by the coincidence detection.

- **Electronics** to process signals from detectors and to communicate with a spacecraft system (not shown in the figure).

First an entering ENA passes through the charged-particle rejector where ambient plasmas are swept out by an electrostatic field. By hitting on the ionization surface, the ENA is ionized with a certain probability, and then the positively-ionized ENA goes through the wave structure where energy analysis is made electrically. The wave structure also works for blocking photons. Entering into the TOF section, the ionized ENA is accelerated by the lens to hit on the START surface.

Collision of ENAs with the START surface creates secondary electrons, which are collected and produce a start signal for a TOF measurement. The ENA particle is scattered after collision, and are finally detected by the STOP MCP to generate a stop signal. By measuring a TOF between the start and stop signals, the velocity of the ENA particle can be acquired.

4   Ionization and START Surfaces

The instrument needs two types of special surfaces, *i.e.*, the ionization surfaces and the START surfaces. The ionization surfaces employ to ionize neutral atoms into positively-charged particles, which enables us to make electric energy analysis. The START surfaces
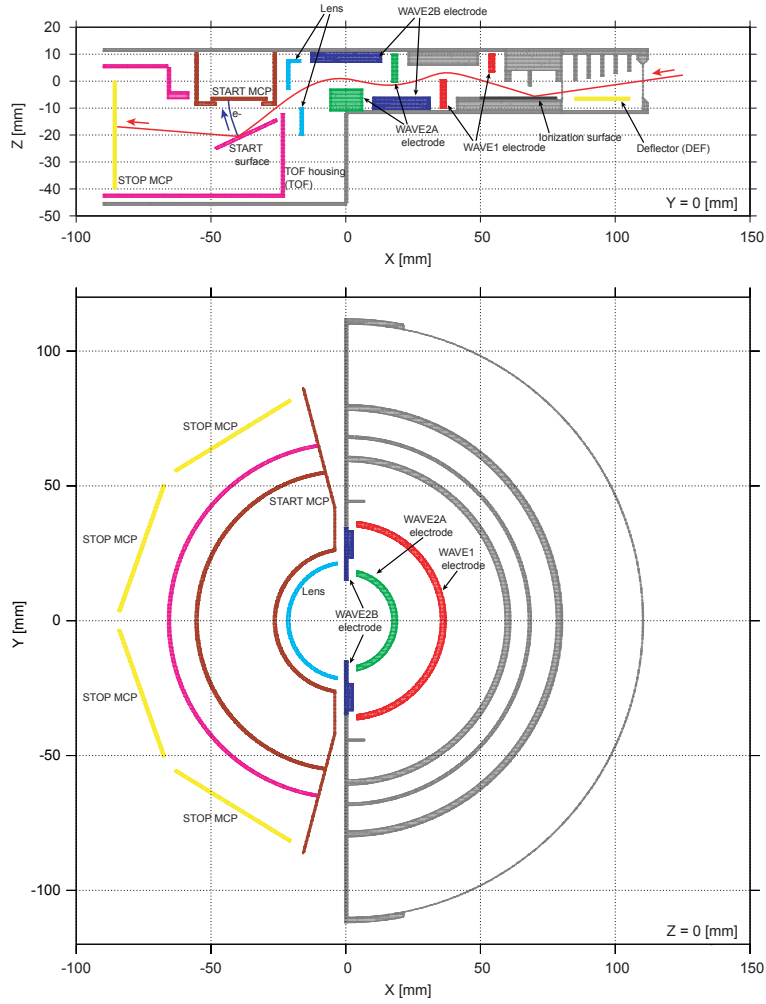
Figure 1: Cut-away view of the sensor. The top panel shows the structures in the XZ plane at $Y=0$, the bottom is in the XY plane at $Z=0$. The sensor is symmetric with respect to the XZ plane.

are used to create secondary electrons which generate a start signal for a TOF measurement.

We will use tungsten-oxide surfaces as the ionization surfaces, according to studies on surface interaction of particles made in University of Bern in Switzerland. Second possibilities are magnesium oxide, silicon oxide, or silicon nitride.

For the START surfaces, a high-Z and flat-surface material is needed for less scattering effects. The START surfaces also require high efficiency of secondary electron creation. In terms of these points, tantalum will be used, and tungsten is a back-up.

5 Time-of-Flight Measurement

The size of the START surface should be large enough to catch more particles. However, a larger START surface compared to the length of TOF path means larger deviations of start positions, resulting in worse TOF resolution.

Not to worsen the resolution, we have introduced an electron mapping method to acquire a position on which electrons are created. A uniform electric field of 300-V difference between the START surfaces and the START MCP collects electrons with position information kept, and multiple anodes on the START MCP detect the creation position of the electrons.

We have introduced four ring anodes and seven sector anodes on the START MCP, and eight rectangular anodes on the STOP MCPs (two for each STOP MCP). The ring, sector, and rectangular anodes are referred to as 'ring', 'sector', and 'plate' anodes, respectively, hereafter for convenience. The anode positions and their numberings are indicated in Figure 2.

Ring and plate anodes are connected to fast amplifiers for a TOF measurement. A ring-to-plate-anode combination gives its flight path. Each sector anode indicates an azimuthal direction of a particle.
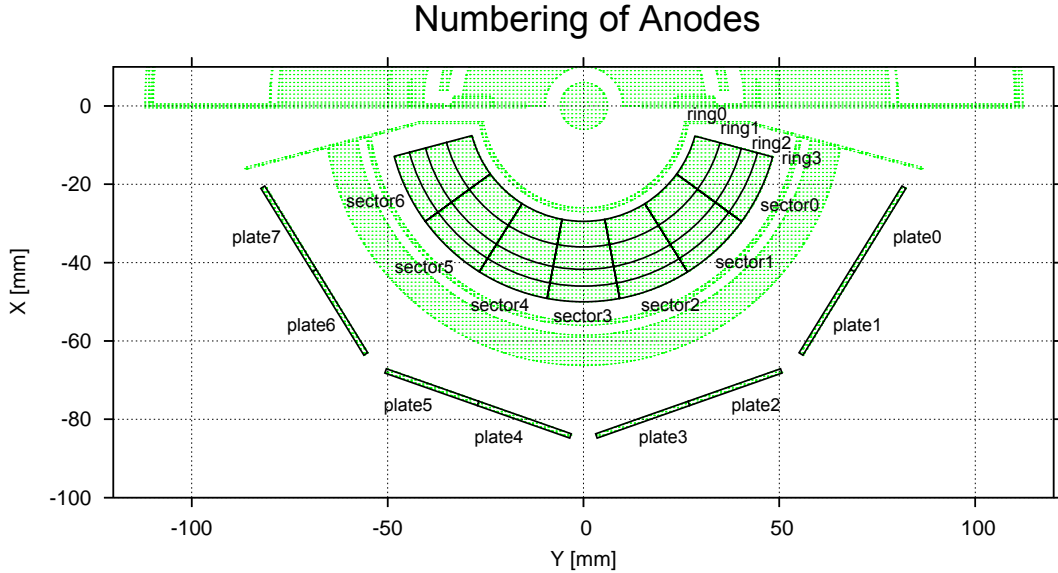

Figure 2: Definitions of anodes on the START and STOP MCPs.

6 Estimation of Mass Resolution

Assuming a simplified configuration as shown in Figure 3, mass resolution of TOF measurement is estimated under a first-order approximation as

$$\left(\frac{\Delta M}{M}\right)^2 \sim \left(\frac{\Delta K}{K}\right)^2 + \left(2\frac{\Delta X}{X}\right)^2 + (2\tan\theta\Delta\theta)^2,$$

where M is a mass, K is an energy, X is a position, θ is an angle of a particle's velocity.
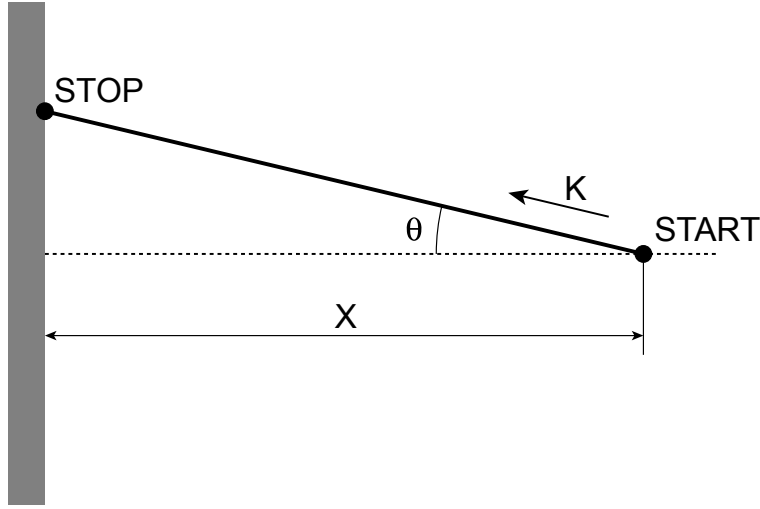

Figure 3: TOF configuration for mass resolution estimation.

For low-energy particles, the energy deviation $\Delta K/K$ is made only by surface scattering which is approximately 15% (FWHM). θ corresponds to an angle of a particle velocity to the STOP MCP and $10\,\deg$ (FWHM) is taken here. the angular deviation $\Delta\theta$ comes from scattering at the TOF start position. X and ΔX are a base-line length and a start position deviation, respectively, and are selected as $X{=}43\,\mathrm{mm}$ (average distance between the MCPs) and $\Delta X{=}8\,\mathrm{mm}$ in FWHM (the half length of the surface).

Each contribution to the mass resolution is summarized in Table 1. Note that a deviation of initial energies is neglected because acceleration before the TOF measurement gives almost same energies to all particles.

The largest error comes from the start position deviation, and this is exactly the reason why we have introduced the electron mapping for start position sensing. By introducing four ring anodes, the mass resolution is estimated as

$$\begin{aligned}
\frac{M}{\Delta M} &\sim \left\{(15\%)^2 + (37\%/4)^2 + (9.2\%)^2\right\}^{-1/2} \\
&= 5.0.
\end{aligned}$$

Item	Error	Remark
$\Delta K/K$	15%	energy deviation
$2\Delta X/X$	37%	start position deviation
$2\tan\theta\,\Delta\theta$	9.2%	angular deviation

Table 1: Errors which contribute to the mass resolution.

The mass resolution of 5.0 enables us to know major groups of components of ENAs, H group, O group, Na/Mg/Al/Si group, K/Ca group, and Fe group.

7 Basics of the Wave Structure

In order to know basic properties of the wave structure, an analytic calculation is made here. We assume a simplified wave structure shown in Figure 4. The upper and lower electrodes face each other with a distance of $2D$, and their potentials are ground. A mesh between the electrodes is applied with a potential ϕ. Electric fields are assumed to be uniform and to be only directed horizontally.

In the structure, a charged particle moves in a parabolic orbit. It is preferable to take an initial releasing angle θ of $45\,\deg$ because of its focusing property. In this case, the distance between mesh-crossings L, and the maximum height h are expressed as

$$L = 2\frac{K}{\phi}D,$$
$$h = \frac{1}{2}\frac{K}{\phi}D,$$

where K is the energy of the particle in eV.

Let the energy of the particle at infinity $K_0(= K - \phi)$ in eV. In order not to hit the electrodes, $h < D$ is needed, then we get the condition $K_0/\phi < 1$. In terms of a large geometric factor, the size of the structure L/D should be as large as possible. This means that a large K_0/ϕ is preferable. On the other hand, higher acceleration ratio K/K_0 is better in the point of view of wider energy passband for higher sensitivity. This condition needs K_0/ϕ as small as possible, contrary to the first condition.

Here we take the value K_0/ϕ of 0.5. In this case, the aspect ratio of the structure L/D becomes 3. We took $18\,\mathrm{mm}$ of L and $6\,\mathrm{mm}$ of D for the instrument.
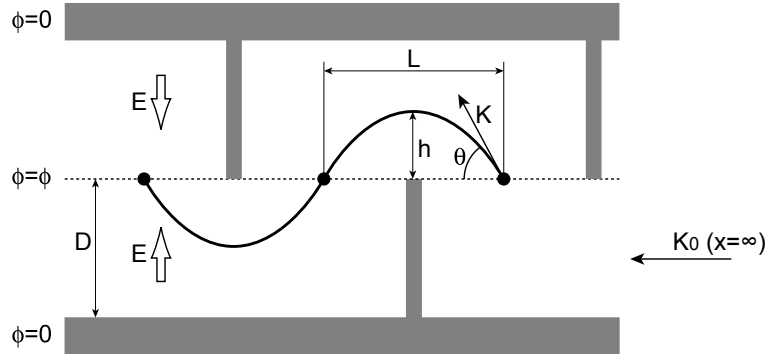
Figure 4: Model wave structure for an analytic calculation.

8 Voltage Setting

8.1 Principle

Inside the sensor exist eight electrodes, DEF (deflector), WAVE1, WAVE2A, and WAVE2B (wave structure), LENS (lens), and TOF (TOF housing), START_MCP (input surface of START MCP), and STOP_MCP (input surface of STOP MCP), from the aperture to the detector. See Figure 1 for the details.

An ENA particle experiences accelerations twice inside the instrument. During passing through the wave structure, the first acceleration takes place to obtain (1) better azimuthal angle resolution especially for low-energy ENAs, and (2) wider energy passband for larger transmittance. This acceleration is made by the electrodes WAVE1, WAVE2A and WAVE2B (mentioned later).

The second acceleration is between the lens and the TOF section. This acceleration contributes for (1) higher efficiency of secondary electron creation on the START surfaces, and (2) better mass resolution for low-energy ENAs by equalizing initial energies at the TOF section.

The electrode DEF is applied with +5000 V to sweep out ambient charged particles all the time the instrument is running. The TOF housing and the START surfaces are set to −2800 V to have grounded anodes on the back side of MCPs. The START MCP's bias voltage is −2500 V. The 300-V potential difference between the START surfaces and the START MCP collects electrons created on the START surfaces. The bias voltage of the STOP MCP is −2850 V, −50 V smaller than that of the TOF housing. This works to repel stray electrons created inside the TOF section.

8.2 Wave Structure

Energy analysis at the wave structure is done by applying appropriate voltages to the electrodes WAVE1, WAVE2A, WAVE2B, and LENS depending on tuning energy. In this section, voltage profiles are described.

Let us assume a simplified wave structure as shown in Figure 5. There are two parts in the structure, and voltage difference exists between them which accelerates particles. The relation between a particle energy and a voltage of the first structure is as follows:

$$K_1 = \alpha(V_{1A} - V_{1B}),$$
$$K_2 = \alpha(V_{2A} - V_{2B}).$$

Here, α is known to be -1.649 according to preliminary simulations. These relations are also written using an energy of a particle at infinity K_0, as

$$K_1 = K_0 + (-V_{1A}),$$
$$K_2 = K_0 + (-V_{2A}).$$

V_{1B} is zero at the actual potential configuration. Therefore, V_{1A} and V_{1B} can be expressed:

$$V_{1A} = (\alpha + 1)^{-1} K_0 = -1.541 \cdot K_0,$$
$$V_{1B} = 0.$$

Next, we think about the second structure. Here we introduce an acceleration parameter β defined as $K_0 + (-V_{2B}) = \beta K_0$, and we set β to 3 in this case. Thus, the potentials can be expressed as:

$$V_{2A} = (\alpha + 1)^{-1}\{1 + \alpha(1 - \beta)\}K_0 = -6.622 \cdot K_0,$$
$$V_{2B} = (1 - \beta)K_0 = -2.000 \cdot K_0.$$

V_{2A} reaches $-5000\,\text{V}$ (the maximum output of HVPS) as particle energies increase to approximately $750\,\text{eV}$ of particle energies. For particles with energies high than $\sim 750\,\text{eV}$, V_{2A} must be kept constant at $-5000\,\text{V}$. Accordingly, the potentials are

$$V_{2A} = -5000,$$
$$V_{2B} = \alpha^{-1}\{(\alpha + 1)V_{2A} - K_0\}$$
$$= -1968. + 0.6064 \cdot K_0.$$

The potential profiles shown above are applied for the actual wave structure as V_{1A} corresponds to V_{WAVE1}, V_{2A} to V_{WAVE2A} and V_{2B} to V_{WAVE2B}.

Finally, the potential of the lens V_{LENS} is defined empirically by computer simulations as follows: V_{LENS} follows V_{WAVE1} until V_{LENS} reaches $V_{\mathrm{TOF}} = -2800\,\mathrm{V}$, then is constant at V_{TOF} for the higher-energy region.

The potential profiles are summarized in Figure 6. It is worthy to address that the potential profiles defined here are derived from analytic calculations, and final profiles should be determined by calibration experiments with an actual model.
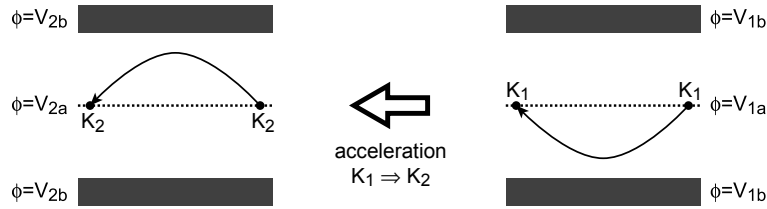

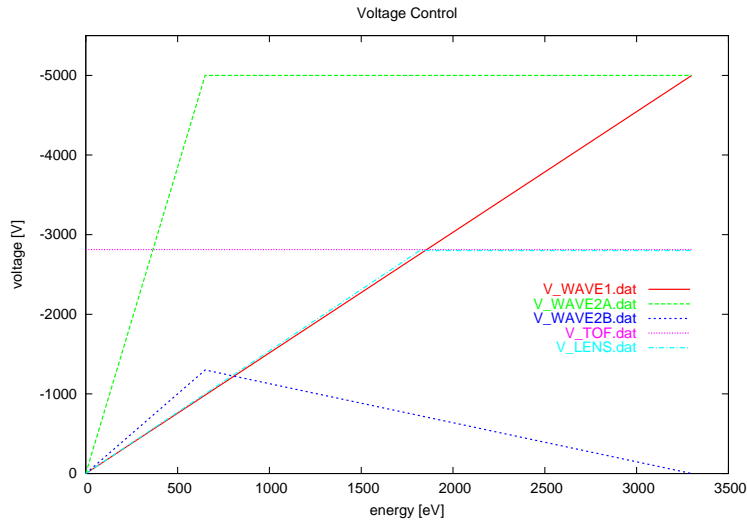Figure 5: Model wave structure which accelerates particles.

Figure 6: Voltage profiles for each anode as a function of tuning energy. Note that the profiles shown are derived from analytical calculations and computer particle tracing. The voltage profiles must be checked by calibration experiments.

9 Trajectory Tracing Code

A computer code has been newly developed for calculations of electric fields and particle trajectories. All calculations are made in three dimensional simulation space. This code can trace trajectories of charged and neutral particles, *i.e.* ions, electrons, neutral atoms,

and photons in electric fields. Instrument performances of photon rejection, ion rejection and ENA measurement are investigated by using the code, which are mentioned later.

Electric fields are calculated in regularly-spaced grids by the successive over relaxation method, and particle tracing is made by the 4th-order Runge-Kutta method with adaptive step-size control. The code is written in C++ and is expandable in an object-oriented way. This capability is applied in the present study to include particle ionization and scattering, photon reflection and electron creation. Then a full trajectory calculation, from the aperture to the detector including an secondary electron can be made with this code.

10   Performance of Photon Rejection

Rejection of photons is one of the crucial points of this instrument, since MCPs are sensitive to photons as well as ENAs. Rejection ratio of photons is obtained by a numerical photon tracing simulation.

On the simulation, two types of photon reflection on a wall are assumed; (1) specular reflection with a reflection coefficient of 10^{-1} on the ionization and the START surfaces, and (2) diffuse reflection with a reflection coefficient of 10^{-2} otherwise.

Photons are injected randomly through the whole aperture within the spin plane (XZ plane) and the photons have no Y-component velocities. This means that the results in this section are integrated over a spin. 5×10^7 photons are injected in the simulation. A fraction of a photon decreases by reflections, and the tracing stops when the fraction of the photon reaches 10^{-10}.

Figure 7 gives histograms of fractions of photons which reach the START MCP, the STOP MCP, or the START surfaces. The fractions are shown logarithmically in the horizontal axes. The results indicate that 2.16×10^{-7} of 5×10^7 photons reach the START MCP. Similarly, 1.10×10^{-2} photons reach the STOP MCP, and 8.32×10^{-5} photons reach the START surfaces. Each rejection ratio of photons is then calculated as:

$$
\begin{aligned}
r_{\text{STA\_MCP}} &= 4.32 \times 10^{-15}, \\
r_{\text{STO\_MCP}} &= 2.20 \times 10^{-10}, \\
r_{\text{STA\_SURF}} &= 1.66 \times 10^{-12}.
\end{aligned}
$$

Therefore, estimated count rates on the START and STOP MCPs due to photons are

$$
\begin{aligned}
c_{\text{STA\_MCP}} &= j_{\text{ph}} \cdot S_{\text{aperture}} \cdot \\
& \quad (r_{\text{STA\_MCP}} \cdot \epsilon_{\text{ph,MCP}} + r_{\text{STA\_SURF}} \cdot \epsilon_{\text{2nd,ele}} \cdot \epsilon_{\text{ele,MCP}}) \\
&= 0.4\,\text{count/sec}, \\
c_{\text{STO\_MCP}} &= j_{\text{ph}} \cdot S_{\text{aperture}} \cdot r_{\text{STO\_MCP}} \cdot \epsilon_{\text{ph,MCP}}
\end{aligned}
$$

$$= \; 60 \, \text{count/sec},$$

where j_{ph} is the photon flux at a Mercury orbit, S_{aperture} is the area of the aperture, $\epsilon_{\text{ph,MCP}}$ and $\epsilon_{\text{ele,MCP}}$ are MCP's detection efficiencies for photons and electrons, respectively. These parameters are assumed as follows: $j_{\text{ph}} = 10^{12} \, /\text{cm}^2 \, \text{sec}$, $S_{\text{aperture}} == 27 \, \text{cm}^2$, $\epsilon_{\text{ph,MCP}} = 1\%$, $\epsilon_{\text{2nd,ele}} = 1\%$, and $\epsilon_{\text{ele,MCP}} = 100\%$.

Finally, a coincidence count rate due to photons can be calculated

$$
\begin{aligned}
c_{\text{ph,coinc}} \quad &\sim \quad c_{\text{STA\_MCP}} \cdot c_{\text{STA\_MCP}} \cdot \tau \\
&= \quad 2 \times 10^{-5} \, \text{count/sec},
\end{aligned}
$$

where τ is a TOF window and is assumed to be 1000 nsec. The count rate estimated is expected to be lower than that of ENAs. This indicates that probably photons do not affect ENA measurements by this instrument.

However, these calculations are obtained numerically by a computer with a model which is not identical to the real sensor structure. It should be emphasized that the photon rejection performance must be verified by laboratory experiments with an actual model.
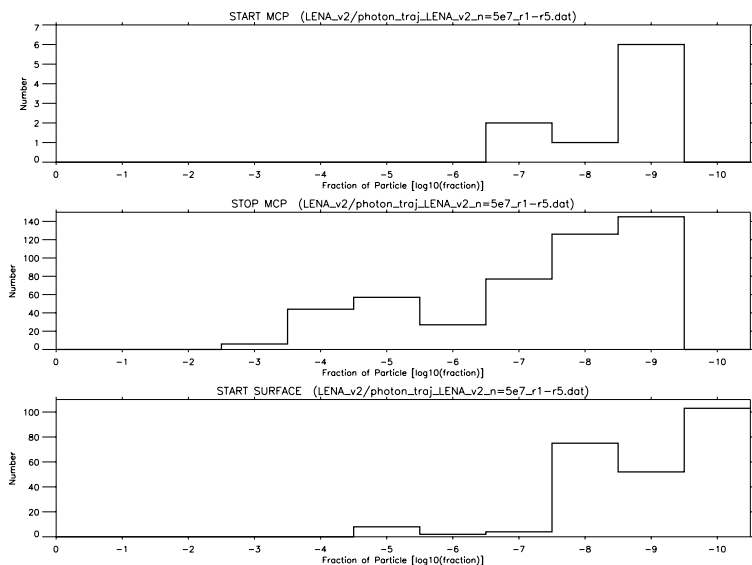

Figure 7: Histograms of fractions of photons which reach the START MCP (top), the STOP MCP (middle), or the START surface (bottom).

11 Performance of Ion Rejection

Ambient ions are swept out by the charged-particle rejector not to be hit on the ionization surfaces. Ions start to hit the ionization surfaces as the energy of the ions increases, and

once they are scattered as ions, the instrument cannot distinguish them from ENAs ionized on the surfaces. Therefore, ion rejection performance is important for ENA measurement.

A rejection ratio of ions is obtained by ion tracing simulations with a sensor model. A rejection ratio is defined as the number of ions which reach the ionization surfaces to the total number of entering ions. The potential of the deflector is applied with $+5000\,\mathrm{V}$ as is a nominal value, and the electrodes of the wave structure are set for 25-eV particles, which means that V_{WAVE1}, V_{WAVE2A}, V_{WAVE2B} are $-38.5\,\mathrm{V}$, $-193.5\,\mathrm{V}$, and $-50.0\,\mathrm{V}$, respectively.

Figure 8 shows the profile of ion rejection ratios calculated by simulations. The profile is normalized to unity at infinity energy by fitting a function. The ratio is approximately 4×10^{-5} at $14\,\mathrm{keV}$, and none of 10^6 particles can reach the surfaces at $13\,\mathrm{keV}$. Therefore, the cut-off energy is between 13 and $14\,\mathrm{keV}$, $\sim 13.5\,\mathrm{keV}$ in conclusion.
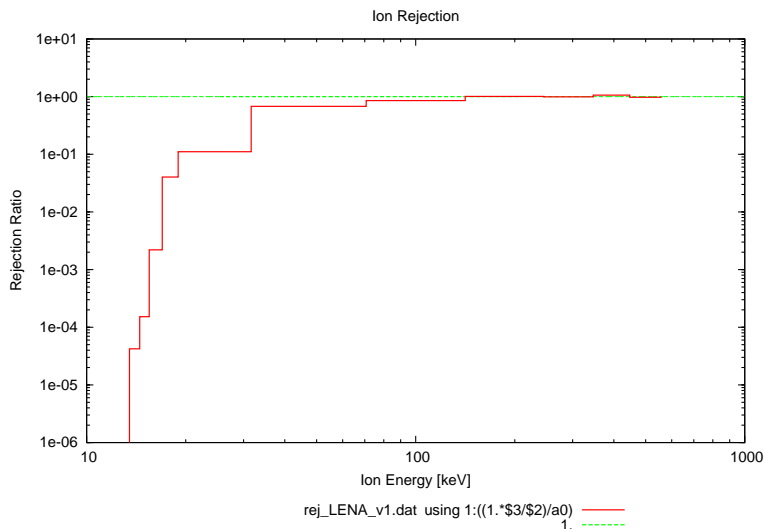

Figure 8: Profile of ion rejection ratios versus ion energy.

12 Performances for ENA Measurement

12.1 Calculation Set-Up

In this section, we show results of computer simulations for estimating ENA measurement performances, such as sensitivities of ENA detection, fields of view, angular resolutions, energy resolutions, mass resolutions.

On the particle tracing, all particle behaviors, ionization and scattering of ENAs on the ionization surface, ENA scattering and secondary electron creation on the START surfaces, are integrated. The scattering model used here is mentioned afterwards.

Tracing of a particle trajectory starts with a randomly-set initial position and a velocity. The initial parameters are recorded if the particle reaches the START surfaces. And then tracing continues for three types of particles, that is to say, neutralized and ionized particles and a secondary electron from the START surfaces. Calculations are repeated until the number of particles which hit on the START surfaces reaches 10000.

The results given in the section will be shown in three different energy tunings, $i.e.$, 25-eV, 750-eV, and 3300-eV cases. Potential setting for each case is tabulated in Table 2.

It should be emphasized that the names of the potential settings such as '25-eV', '750-eV', and '3300-eV' cases are symbolic (theoretically derived) and do not stand for their mean energies. In fact, There are slight differences between the named energy and the calculated energy (see the later section).

Electrode	Voltage [V]		
	25-eV case	750-eV case	3300-eV case
WAVE1	−38.5	−1136	−5000
WAVE2A	−193.0	−4500	−5000
WAVE2B	−50	−1536	−0
LENS	−38.5	−1136	−2800
TOF	−2800	−2800	−2800
START_MCP	−2500	−2500	−2500
STOP_MCP	−2850	−2850	−2850

Table 2: Potential settings of electrodes for 25-eV, 750-eV, and 3300-eV tuning cases.

Figure 9 displays a potential distribution in the 25-eV case. Note that no STOP MCPs are shown in the figure since the potential is drawn in the plane of $Y=0$ which does not contain the STOP MCP. The model sensor structure in the simulation space is divided into two regions (shown as two rectangles in the figure) to save computer's memory on calculation.

12.2 Model of Particle Scattering

The model of particle scattering on the surfaces used in the simulation is based on Andrei's model [*personal communication*]. The scattering model defines momenta of scattered particles, $i.e.$, a final energy, and exiting directions as functions of an initial energy and initial elevation angles. Hereafter we denote energy, elevation angle and azimuthal angle by K, EL and AZ, respectively. The elevation angle is the angle of from the surface, and the azimuthal angle is the direction within the surface plane.
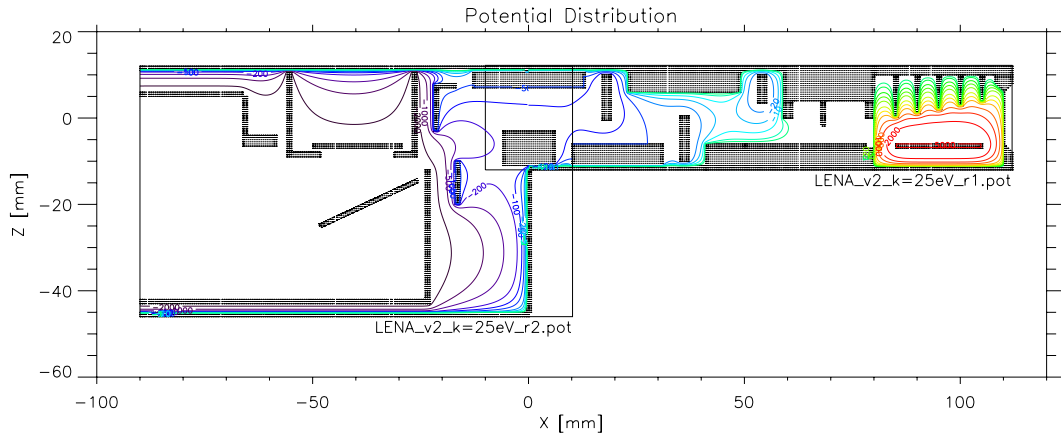
The model is based on several assumptions:

Figure 9: Potential distribution in the case of 25-eV tuning.

- Scattering properties do not depend on species of incident particles.

- Ionization efficiency is constant at 10% and does not depend on other parameters.

- Elevation and azimuthal angles of scattered particles are determined only by their initial elevation angles.

- Deviations of elevation and azimuthal angles of scattered particles are defined identically.

- Final average energies and stragglings are determined only by their initial energies.

Energy loss and straggling are modeled as shown in Figure 10. In the model, energy loss and straggling are proportional to initial energy, 13% and 25% of the initial energies, respectively. Those properties agree with *Martin et al.* [2002][1]. Therefore, the average and residual energies of scattered particles, $\langle K_1 \rangle$ and $\sigma(K_1)$ are expressed obviously as:

$$\langle K_1 \rangle = 87\% \cdot K_0,$$
$$\sigma(K_1) = 25\% \cdot K_0,$$

where K_0 means initial energies of particles.

Averages and deviations of elevation and azimuthal angles of exiting particles are displayed in Figure 11. Two data points at an initial elevation angle of zero have been added to Andrei's model; (1) 10 deg of the angle deviation and (2) 0 deg of the average angle.

---

[1]M. Wieser *et al.*, Nucl. Instr. and Meth. in Phys. Res., B 192 (2002) 370–380

Since Andrei's model only gives discrete data points, the data are fitted to analytic expressions for interpolation and extrapolation. Then we get the profiles as:

$$\langle EL_1 \rangle = 0.05147 \cdot (EL_0)^2 + 8.160,$$
$$\sigma(EL_1), \sigma(AZ_1) = 2.332 \cdot (\sqrt{EL_0 + 1} - 1),$$

where EL_0 means initial elevation angles of particles, and all angles are represented in degrees. Note that the fitting functions are selected only for data interpolation and do not have any scientific meaning.
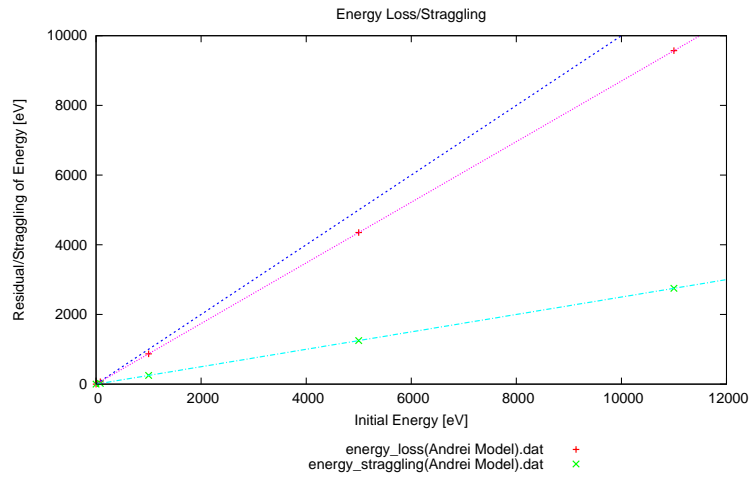

Figure 10: Model profiles of energy loss and straggling of scattered particles.

12.3 Model of Secondary Electron Creation

Collision of particles on the START surfaces results in creation of secondary electrons. Since the ENA instrument uses secondary electrons for a start signal of a TOF measurement, a secondary electron emission model is needed for the simulations.

The model used in this study is as follows:

- Electrons are emitted uniformly in the elevation and azimuthal directions, *viz.*, $EL, AZ \longleftarrow$ random numbers.

- Initial energies of electrons are distributed equally from 0 to 5 eV.

In the calculations, the efficiency of secondary electron creation is assumed to 1 (one electron always).
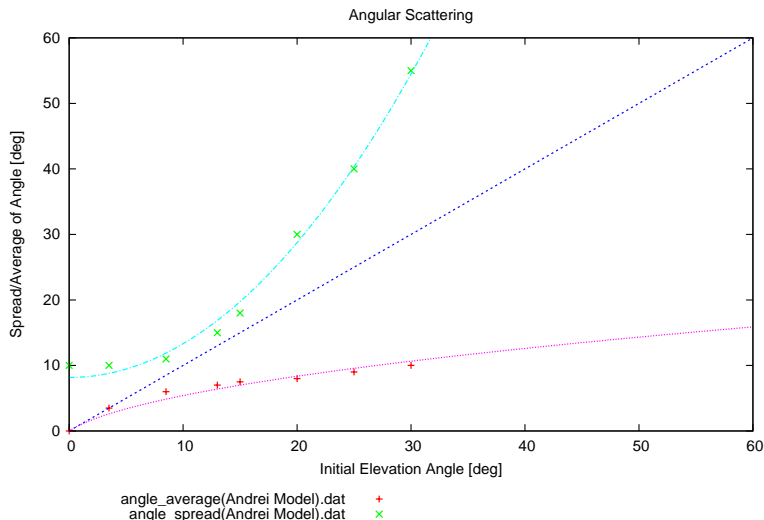
Figure 11: Model profiles of average and deviation of elevation/azimuthal angles of scattered particles.

12.4 Sensitivity

Sensitivities of ENA measurement are mentioned in this section. Here a sensitivity is defined as a product of a geometric factor and efficiencies.

First, let us think about efficiencies. The sensor has several factors which reduce the number of particles to be detected, that is, (1) transmittances of the two meshes, (2) ionization ratio on the ionization surfaces, (3) ratio of secondary electron creation on the START surfaces, (4) reflection efficiency on the START surfaces, and (5) detection efficiency of MCPs. These efficiencies are assumed as shown in Table 3.

Item		Efficiency
Mesh transmittance	ϵ_{mesh}	90%
Ionization	ϵ_{ion}	10%
Electron creation	$\epsilon_{\mathrm{2nd,ele}}$	100%
Surface reflection	ϵ_{ref}	5%
MCP detection for ENA	$\epsilon_{\mathrm{ENA,MCP}}$	60%
MCP detection for electron	$\epsilon_{\mathrm{ele,MCP}}$	100%

Table 3: Efficiencies of each factor.

Therefore, the overall efficiency ϵ becomes

$$\epsilon = \epsilon_{\mathrm{mesh}}^2 \cdot \epsilon_{\mathrm{ion}} \cdot \epsilon_{\mathrm{2nd,ele}} \cdot \epsilon_{\mathrm{ref}} \cdot \epsilon_{\mathrm{ENA,MCP}} \cdot \epsilon_{\mathrm{ele,MCP}} = 0.243\%$$

16

Next, geometric factors are calculated by the simulations. Here geometric factors are calculated for particles which satisfy both (1) the secondary electron reaches the START MCP and (2) the particle reaches the STOP MCP.

Tables 4, 5, and 6 summarize geometric factors calculated for 25-eV, 750-eV and 3300-3eV cases, respectively, with overall sensitivities which is a product of a geometric factor with the overall efficiency of 0.243%. The geometric factor is integrated over energy, which is automatically made in the Monte-Carlo method. The two types of geometric factors are shown in each table, one is for particles which are neutralized on the START surfaces (major component), the other is for particles which are not (minor component).

The center channel (sector #3) shows a slightly smaller geometric factor because the gap between the STOP MCPs exists in front of the channel, and some of particles are lost in the gap.

Geometric factors calculated only with the START MCPs (a particle is taken into account even if the particle is not detected by the STOP MCPs) show up to ∼26% higher values in the case of neutralized particles (these results are not shown here). This comes from scattering of particles on the START surfaces.

Sector	Pure G-factor [cm^2 sr eV]	Overall G-factor [cm^2 sr eV]	Pure G-factor [cm^2 sr eV]	Overall G-factor [cm^2 sr eV]
	Neutralized on scattering		Ionized on scattering	
0	0.682	1.66×10^{-3}	0.696	1.69×10^{-3}
1	1.228	2.98×10^{-3}	1.520	3.69×10^{-3}
2	1.441	3.50×10^{-3}	1.500	3.65×10^{-3}
3	1.259	3.06×10^{-3}	1.549	3.76×10^{-3}
4	1.486	3.61×10^{-3}	1.555	3.78×10^{-3}
5	1.239	3.01×10^{-3}	1.523	3.70×10^{-3}
6	0.635	1.54×10^{-3}	0.645	1.57×10^{-3}

Table 4: Geometric factors in the case of the 25-eV setting.

12.5 Angular Properties

12.5.1 Elevation Angle Response

A elevation-angle response is displayed in Figure 12. The data shown are for the case that the electrodes are set for 25-eV ENAs. The field-of-view (FOV) in elevation angle is defined geometrically with upper baffles and the deflection electrode at the charged-particle rejector part. The FOV ranges from 0 to 19.8 deg according to the design, and the simulation result agrees well with those figures. The elevation-angle resolution is ∼10 deg

Sector	Pure G-factor [cm^2 sr eV]	Overall G-factor [cm^2 sr eV]	Pure G-factor [cm^2 sr eV]	Overall G-factor [cm^2 sr eV]
	Neutralized on scattering		Ionized on scattering	
0	6.424	$1.56{\times}10^{-2}$	6.733	$1.64{\times}10^{-2}$
1	8.647	$2.10{\times}10^{-2}$	10.899	$2.65{\times}10^{-2}$
2	12.695	$3.08{\times}10^{-2}$	12.825	$3.12{\times}10^{-2}$
3	9.675	$2.35{\times}10^{-2}$	12.346	$3.00{\times}10^{-2}$
4	12.112	$2.94{\times}10^{-2}$	12.341	$3.00{\times}10^{-2}$
5	8.696	$2.11{\times}10^{-2}$	10.829	$2.63{\times}10^{-2}$
6	6.248	$1.52{\times}10^{-2}$	6.606	$1.61{\times}10^{-2}$

Table 5: Geometric factors in the case of the 750-eV setting.

Sector	Pure G-factor [cm^2 sr eV]	Overall G-factor [cm^2 sr eV]	Pure G-factor [cm^2 sr eV]	Overall G-factor [cm^2 sr eV]
	Neutralized on scattering		Ionized on scattering	
0	7.231	$1.76{\times}10^{-2}$	7.318	$1.78{\times}10^{-2}$
1	9.100	$2.21{\times}10^{-2}$	11.461	$2.79{\times}10^{-2}$
2	10.757	$2.61{\times}10^{-2}$	10.857	$2.64{\times}10^{-2}$
3	8.249	$2.00{\times}10^{-2}$	10.538	$2.56{\times}10^{-2}$
4	10.017	$2.43{\times}10^{-2}$	10.283	$2.50{\times}10^{-2}$
5	9.166	$2.23{\times}10^{-2}$	11.832	$2.88{\times}10^{-2}$
6	6.998	$1.70{\times}10^{-2}$	7.020	$1.71{\times}10^{-2}$

Table 6: Geometric factors in the case of the 3300-eV setting.

(FWHM), which is sufficient for the measurement of ENAs originating from surfaces of planets. The other results in the 750-eV and 3300-eV cases show identical profiles (not shown).

12.5.2 Azimuthal Angle Response

This section describes fields-of-view (FOVs) and resolutions in azimuthal angle. Resolving azimuthal-angle directions of ENAs are made to detect secondary electrons by sector anodes of the START MCP. The seven sector anodes are placed on the backside of the START MCP at every 21.5 deg to cover ±75.25 deg, and each of them corresponds to an azimuthal direction of an ENA.

Three data plots shown here are azimuthal-angle distributions for each sector anode of the START MCP on which particles hit. As well as other results, three different settings
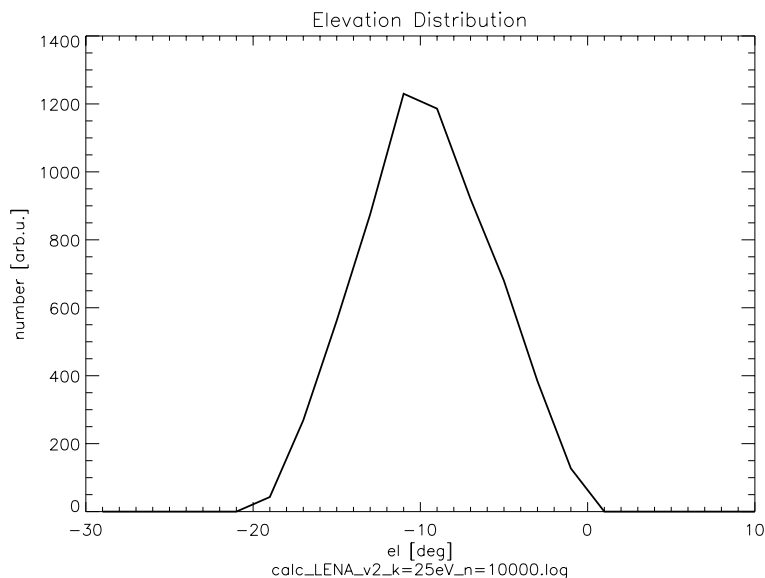
Figure 12: Response in elevation angle in the case of the 25-eV tuning.

of the electrodes, 25-eV, 750-eV and 3300-eV cases, are taken.

Figure 13 displays distributions in the 25-eV case. The azimuthal-angle resolutions are roughly 25 deg (FWHM) at the center sector, and 30 deg at the side sectors (FWHM). The FOV is approximately ±75 deg (between the half-maximum points on the both ends). This FOV agrees well with the coverage of the START-MCP anodes.

Tails are seen in the distributions of two sector anodes on the both sides (#0 and #6). The cause of the tails is an electric field in the center region of the sensor. This point will be discussed later.

Calculation results in the 750-eV case are shown in Figure 14. The angular resolutions are 40–45 deg, larger than those in the 25-eV case. The FOV is about ±70 deg.

It is seen in the data that the distributions on the both ends are shifted toward the center, and have worse resolutions compared to the others. This brings those distributions to be almost included in their neighboring distributions. Thus, those two sectors become less important in terms of azimuthal-angle resolutions. This is also due to the electric field in the center region.

Figure 15 shows the data in the case of the 3300-eV setting. In this setting, the resolutions are 25–30 deg, and the FOV is approximately ±63 deg. The sectors on the both sides are also included in their neighboring distributions similarly in the 750-eV case.

About angular resolutions, the resolutions in the 750-eV case is worse than the others. This probably comes from a degree of particle acceleration. In low-energy cases such as the 25-eV case, the acceleration works to help a particle reach the anode which the particle
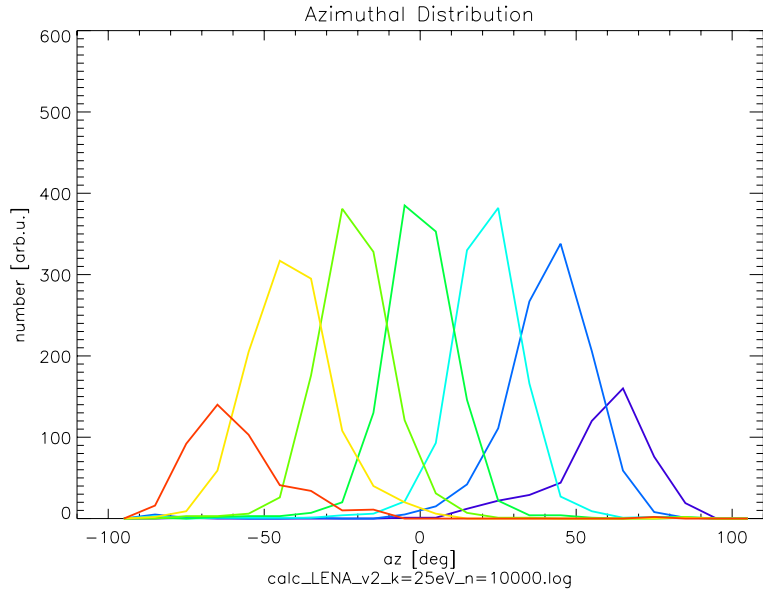
19

Figure 13: Azimuthal-angle response for each sector on the START MCP. The results are calculated in the potential setting for 25 eV.
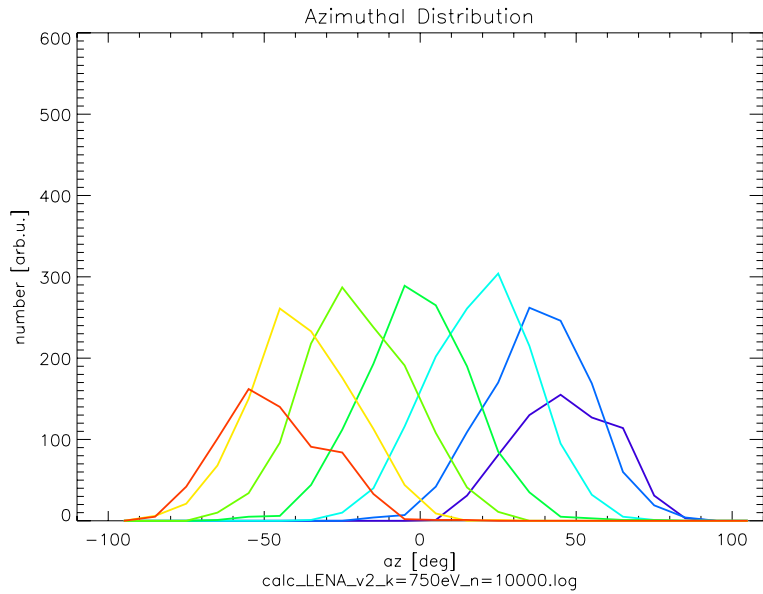

Figure 14: Azimuthal-angle response for each sector on the START MCP. The results are calculated in the potential setting for 750 eV.

is supposed to reach. On the other hand, in high-energy cases, the acceleration no longer changes the trajectories of particles, resulting in geometrically-defined resolutions which
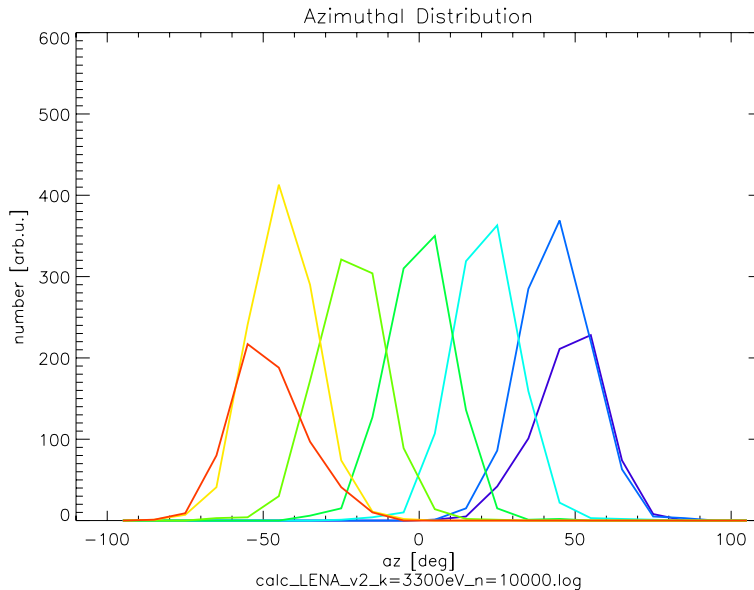
Figure 15: Azimuthal-angle response for each sector on the START MCP. The results are calculated in the potential setting for 3300 eV.

are comparatively better than those in middle-energy cases.

The azimuthal-angle response is highly sensitive to electric field distributions. A complicated electric field is created around the center of the sensor by the voltages of V_{WAVE2A}, V_{WAVE2B} and V_{LENS}. The field strongly affects particle trajectories. Therefore, detailed calculations and/or careful experiments are required to improve the angular performances. Examples of particle trajectories are shown later.

12.6   Energy Bandwidth

Initial energy distributions of particles are also calculated for the 25-eV, 750-eV, and 3300-eV cases as shown in Figures 16–18. From the results, peak energy (K), energy width (ΔK) and energy resolution ($\Delta K/K$) are summarized as in Table 7.

Voltage setting	Peak energy [eV]	Energy width [eV], FWHM	Resolution
25-eV case	$\sim$28	$\sim$30	$\sim$107%
750-eV case	$\sim$800	$\sim$650	$\sim$81%
3300-eV case	$\sim$3000	$\sim$2100	$\sim$70%

Table 7: Peak positions, widths and resolutions of energy distributions.

The positions of peaks and widths are read by hand. An average energy will be slightly higher than its peak value because of the tail in the higher-energy region. The energy resolution decreases as the tuning energy increases. This reflects an acceleration effect which is more effective for lower-energy particles.

The energy distributions are asymmetric, due to the high-energy tail. There are probably two reasons for the tail; (1) vertical overlap between the wave-structure electrodes, and (2) gaps of the wave-structure final electrode to the separation wall.

The vertical overlap between the upper and lower electrodes of the wave structure is 1 mm, which is small compared to 12 mm of the vertical height of the structure. This small overlap allows high-energy particles to pass through the structure in very shallow paths.

The other reason arises from gaps of the innermost electrode in the wave structure. The electrode ends just before the center wall which separates the wave structure and the TOF part. Relatively high-energy particles can go through the gaps and are less discriminated in energy. This effects explains the tail especially in the very high-energy region. This point is mentioned later with examples of trajectories.
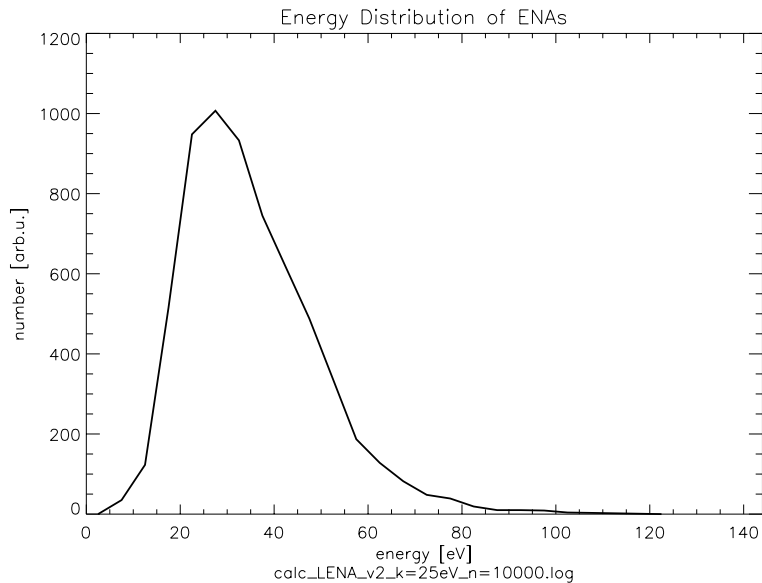

Figure 16: Distribution of initial energies in the 25-eV case.

12.7 Dependence of START-STOP Anodes

Here dependence of anodes between START and STOP MCPs are mentioned. The dependence means that which STOP-MCP anode is related to which START-MCP anode through particles.

Figure 19 represents numbers of particles as a function of both START and STOP
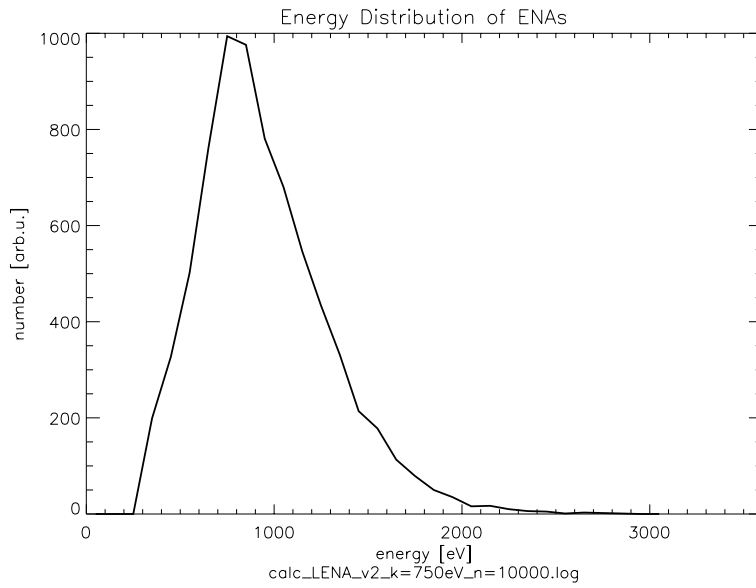
Figure 17: Distribution of initial energies in the 750-eV case.
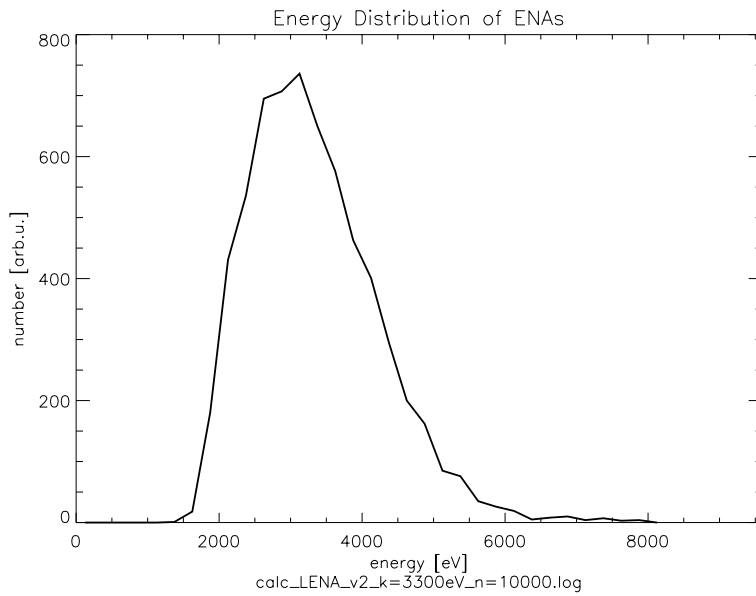

Figure 18: Distribution of initial energies in the 3300-eV case.

anodes. The shown results are for non-ionized particles on the START surfaces in the 25-eV case, but other cases (different energies, different charge states) show same results because scattering directions do not depend on either energy or charge state in the used model.

It is seen that in principle particles go to two STOP-MCP anodes facing the START-MCP anode on which the particles create signals. This result may simplify signal processing in the electronics.
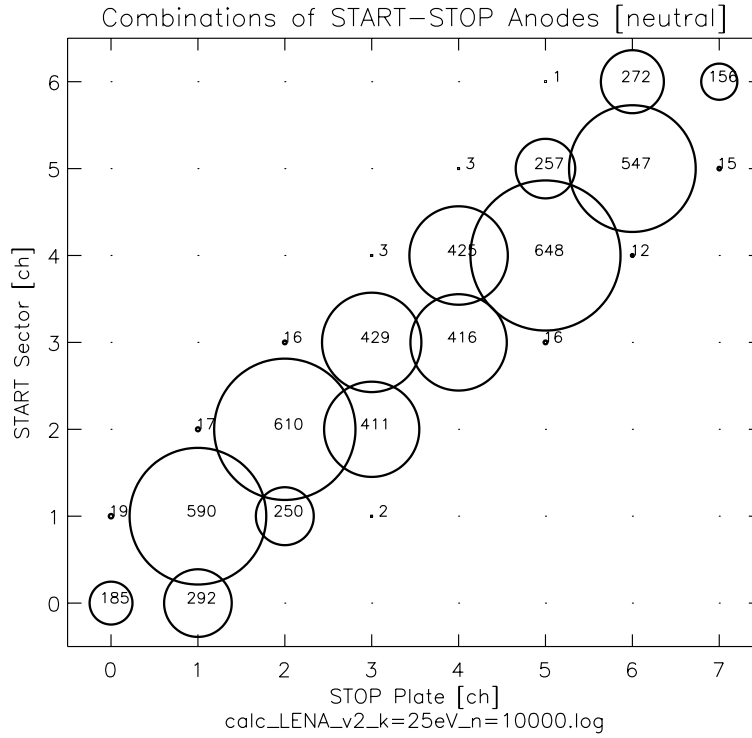
Figure 19: Dependence of anodes between the START and STOP MCPs.

12.8   Mass Discrimination

Examples of calculated TOF distributions for major species are shown in Figure 20 (25-eV case) and Figure 21 (3300-eV case). Those distributions are taken from the data of #3 sector anode and #4 plate anode. Each figure has four TOF distributions which correspond to ring anodes #0–#3. The data shown here are for particles neutralized after START-surface scattering, and there are no differences in the results between neutralized and ionized particles.

As seen in the figures, TOF distributions range up to ∼700 nsec in the 25-eV case, and to ∼500 nsec in the 3300-eV case. The 25-eV result shows slightly better mass resolutions than the 3300-eV case because 25-eV particles are accelerated by 2800 V before TOF measurements and their energy deviation is much reduced.

The mass resolution roughly seems to be 3 or less, and it is obvious that the instrument does not distinguish heavy species, for example, Na from Mg, K from Ca. However,

24

information about mass groups, such as Na/Mg group and K/Ca group, can still be obtained from the instrument. Considering limitations on the instrument, especially the weight limitation of 2 kilograms, we conclude that this mass resolution is satisfactory from the scientific point of view.
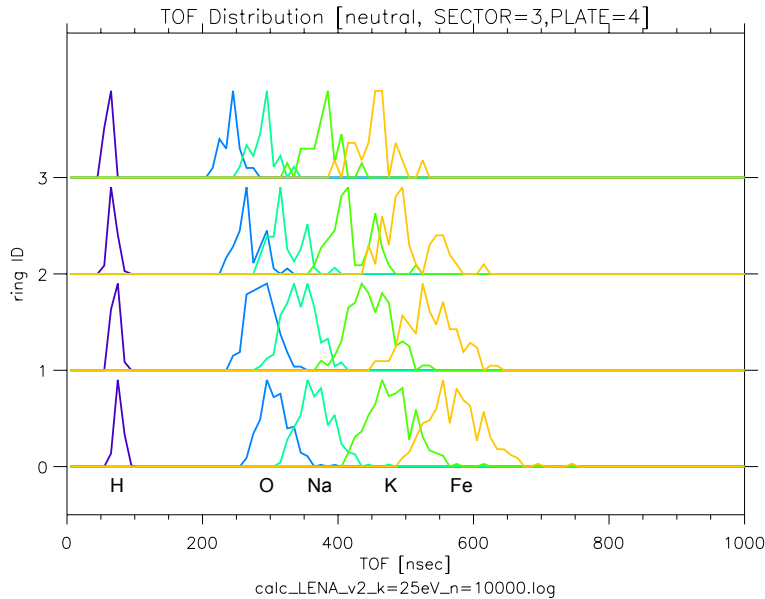

Figure 20: TOF distributions for the ring anodes in the case of 25-eV setting. TOF data of #3 sector anode and #4 plate anode are plotted representatively.

12.9 Examples of Particle Trajectories

12.9.1 Azimuthal Angle Response

Here trajectories of particles are shown which degrade azimuthal angle resolutions.

Figure 22 displays trajectories of particles which have initial azimuthal angles less than 30 deg and finally reach #0 sector anode of the START MCP (see the right-hand panel in the figure). The electrodes are set for the 25-eV tuning. The particles are repelled by the voltage WAVE2A of -193.0 V at an inner wall electrode, and are then repelled by the other inner wall again. Finally the particles go to the START surfaces to create electrons to be detected by #0 sector anode. This causes a tail in the azimuthal angle distribution for #0 sector anode (as seen in the other panel in the figure). The same effect is also seen in #6 anode data because of symmetry of the sensor.

Also are seen another type of trajectories which are reflected inward. The particles are coming in opposite directions and are ionized on the ionization surfaces. After being ionized and reaching the second mesh, they are repelled by the $+5000$-V electric field
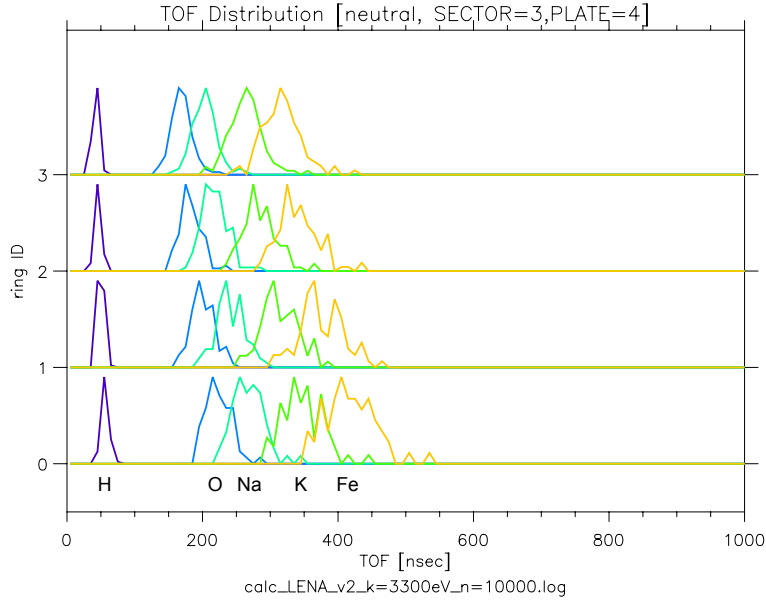
Figure 21: TOF distributions for the ring anodes in the case of 3300-eV setting. TOF data of #3 sector anode and #4 plate anode are plotted representatively.

in the charged particle deflector. One of the particles passes a gap between the last wave-structure electrode and the inner wall, and then reflection occurs in the same way. The number of these particles are not large and they do not change the azimuthal angle distributions largely. However, it is important to keep in mind that such trajectories exist.

Figure 23 shows trajectories of particles whose initial azimuthal angles are less than 20 deg and reach #0 sector anode in the 750-eV case. Particles, which should go to #2 sector anode, finally reach #0 sector anode due to the electric field at the center of the sensor. This particle deflection makes the angular distribution of #0 sector anode worse. The same effect is also seen in the 3300-eV case as seen in Figure 24.

In order to maximize the effective sensitivity area, the sensor accelerates particles inward at the front part of the sensor (at the wave structure) and outward at the rear part (at the lens). Thus, the electric field is not straightforward at the center region of the sensor which is enclosed by the WAVE2A/WAVE2B electrodes, the lens, and the inner walls.

This focusing property works fine for low-energy neutrals such as 25-eV ENAs to obtain the good azimuthal-angle resolutions. However, this does not always work over the whole energy range. Figure 25 displays trajectories of particles which have initial azimuthal angles more than 30 deg and are detected by #3 sector anode in the 750-eV case.

It is seen that particles are accelerated toward the center at the wave structure and then they are accelerated away from the center, resulting in the large bending of the
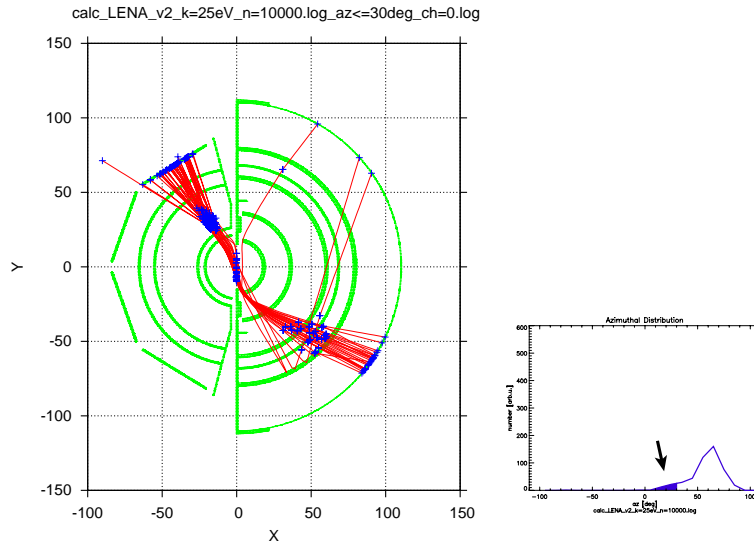
26

Figure 22: Trajectories of particles which have initial azimuthal angles less than 30 deg and are detected by #0 sector anode in the 25-eV case.
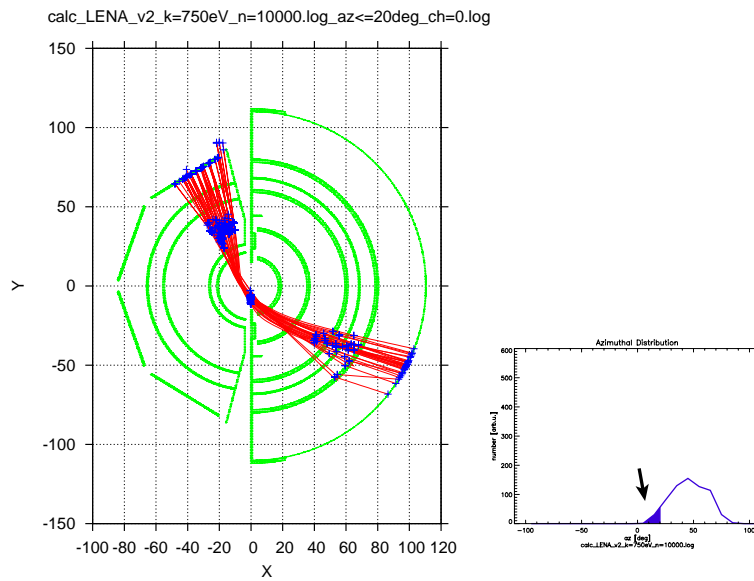

Figure 23: Trajectories of particles which have initial angles less than 20 deg and are detected by #0 sector anode in the 750-eV case.

trajectories.

As seen in the figures shown in this section, the electric field distribution in the center region of the sensor drastically changes trajectories of particles, which is crucial for az-
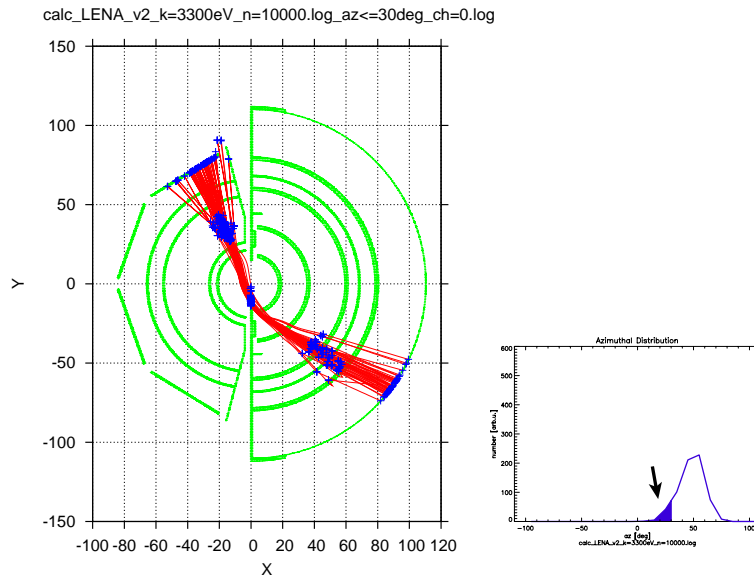
Figure 24: Trajectories of particles which have initial angles less than 30 deg and are detected by #0 sector anode in the 3300-eV case.
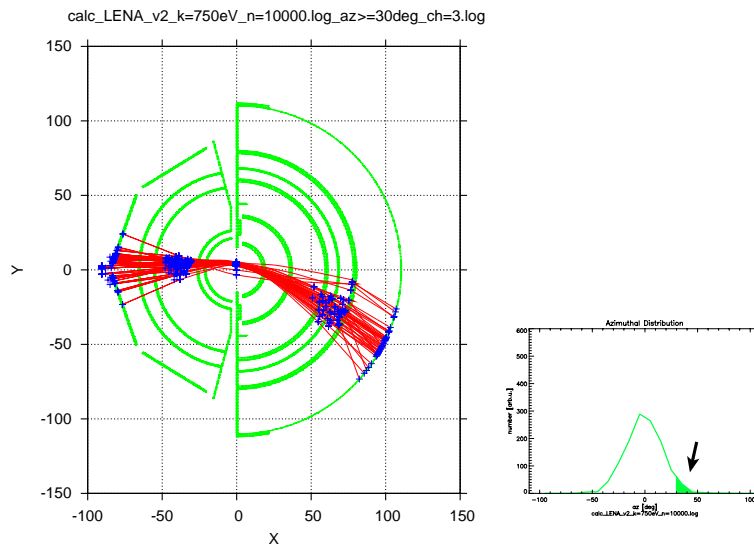

Figure 25: Trajectories of particles which have initial azimuthal angles more than 30 deg and are detected by #3 sector anode in the 750-eV case.

imuthal angle resolutions. Another voltage set-up might bring better angular resolutions. However, no detailed search for optimal voltage setting has been made yet.

12.9.2 High-Energy Tail

The high-energy tail in the energy distribution is discussed here in terms of trajectories of particles. Trajectories of particles with the energies more than 7000 eV in the 3300-eV case are given in Figure 26. Two types of trajectories are seen in the figure.

One is particles which pass through gaps between the innermost wave-structure electrode and the separation walls (the gaps are indicated by circles in the figure). Skipping the electrode means less energy analysis done, resulting in the high-energy tail in the distributions. We can close the gaps with resistive parts if it is strongly needed.

The other is particles going horizontally in the figure. Those particles pass the wave structure with grazing the electrodes. This type of particles can be eliminated if necessary by increasing the vertical overlap of wave electrodes (which is ±0.5 mm in the current design).

However, we conclude that those high-energy tails do not affect much in ENA observation because the number of the particles in the tail is not large, and energy resolution is less important in terms of scientific objectives.
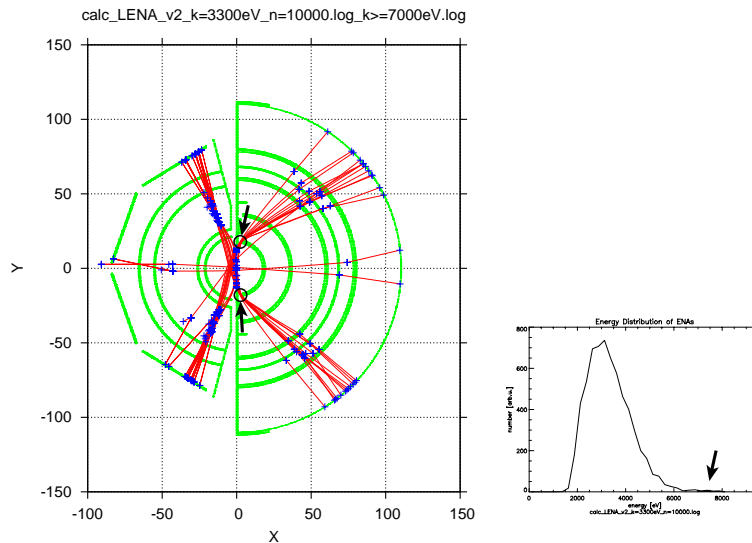

Figure 26: Trajectories of particles with initial energies more than 7000 eV in the 3300-eV case.

13   Remarks

The present report describes performances of the ENA instrument obtained by numerical particle-tracing simulations. Development of a prototype model of the instrument is now ongoing, and performance verification will be made soon with the prototype model.

Because the detection techniques employed in this instrument are highly complicated and their properties cannot be easily predicted, a combination of experiments with computer simulations will be needed on developing the instrument. The author hopes this report will help the development of the instrument.